Ion Velocity Characterization of the 12.5-kW Advanced Electric Propulsion System Engineering Hall Thruster

Wensheng Huang[*], Jason D. Frieman[†], Hani Kamhawi[‡], and Peter Y. Peterson[§]
National Aeronautics and Space Administration Glenn Research Center, Cleveland, OH, 44135, USA

Richard R. Hofer[**]
Jet Propulsion Laboratory, California Institute of Technology, Pasadena, CA, 91109, USA

During development testing of the 12.5-kW Advanced Electric Propulsion System engineering unit Hall thruster, which is magnetically shielded, a laser-induced fluorescence test was performed. During this test, a third medium-energy ion population was found near the inner front pole cover in addition to two low-energy counter-streaming ion populations that were found in previous testing. This newly found ion population matched in characteristics with the single population found near the outer front pole cover. The measured characteristics of the medium-energy ions matched the behavior expected of them if they were energized by a plasma wave with magnetized electrons, such as a lower hybrid wave. Comparison of the data from this test to prior tests showed that this engineering thruster had very similar ion characteristics as the precursor laboratory thruster. The acceleration zone was found to move upstream with increasing background pressure, decreasing anode flow rate, and increasing magnetic field strength. For the low-energy ions, the energy of the ions arriving at the inner pole did not vary noticeably with background pressure but did increase with increasing magnetic field strength and decreasing anode flow rate. For the medium-energy ions, the energy of the ions increased with decreasing background pressure, decreasing anode flow rate, and increasing magnetic field strength. Testing at different cathode flow fraction showed that the energy of the low-energy ions from the cathode decreased with increasing cathode flow.

Abbreviations

AEPS	=	Advanced Electric Propulsion System	IPS	=	Ion Propulsion System
AOI	=	Angle of incidence	JPL	=	Jet Propulsion Laboratory
AR	=	Aerojet-Rocketdyne	LIF	=	Laser-Induced Fluorescence
EP	=	Electric Propulsion	OFPC	=	Outer Front Pole Cover
ETU	=	Engineering Test Unit	RFC	=	Reference Firing Condition
FWHM	=	Full-Width-at-Half-Maximum	SEP	=	Solar Electric Propulsion
GRC	=	Glenn Research Center	SNR	=	Signal-to-Noise Ratio
HALO	=	Habitation and Logistics Outpost	STMD	=	Space Technology Mission Directorate
HERMeS	=	Hall Effect Rocket with Magnetic Shielding	TDM	=	Technology Demonstration Mission
			TDU	=	Technology Development Unit
IFPC	=	Inner Front Pole Cover	VF	=	Vacuum Facility

[*] Research Engineer, Electric Propulsion Systems Branch, AIAA Associate Fellow, wensheng.huang@nasa.gov.
[†] Research Engineer, Electric Propulsion Systems Branch, AIAA Member.
[‡] Research Engineer, Electric Propulsion Systems Branch, AIAA Associate Fellow.
[§] SEP Project Lead Engineer, Electric Propulsion Systems Branch, AIAA Associate Fellow.
[**] AEPS Thruster Lead and Supervisor, Electric Propulsion Group, AIAA Associate Fellow.

I. Introduction

NASA continues to evolve a human exploration approach for beyond low-Earth orbit and to do so, where practical, in a manner involving international, academic, and industrial partners [1]. The center of this approach is NASA's Gateway that is envisioned to provide a maneuverable outpost in lunar orbit to extend human presence in deep space and expand on NASA's exploration goals. The Gateway represents the initial step in NASA's architecture for human cislunar operations, lunar surface access, and missions to Mars.

Figure 1. NASA concept of the PPE and HALO.

NASA announced at the May 2020 NASA Advisory Council's Human Explorations and Operations Committee a new plan that calls for launching the first two elements of Gateway as a co-manifested mission in the late 2023 timeframe [2]. Launching the Power and Propulsion Element (PPE) and the Habitation and Logistics Outpost (HALO) together reduces mission risk, utilizes the PPE high-power Electric Propulsion (EP) system to transport both elements to the lunar orbit, and reduces overall cost. NASA and Maxar Technologies have a commercial partnership to develop and demonstrate a high-power Solar Electric Propulsion (SEP) spacecraft [3, 4]. The PPE is baselined to include three 12.5-kW Advanced Electric Propulsion Systems (AEPS) thrusters, developed by Aerojet Rocketdyne (AR) and four 6-kW Hall thrusters, developed by Maxar.

High-power SEP is one of the key technologies that has been prioritized because of its significant exploration benefits, specifically, for missions beyond low Earth orbit. Spacecraft size and mass are currently dominated by onboard chemical

Figure 2. HERMeS TDU (left) with AEPS ETU (right).

propulsion systems and propellants that may constitute more than 50 percent of spacecraft mass. The propulsion system impact can be substantially reduced through the utilization of SEP, due to its higher specific impulse and lower propellant load required to meet the equivalent mission delta-V. Studies performed for NASA's Human Exploration and Operations Mission Directorate (HEOMD) and Science Mission Directorate (SMD) have demonstrated that 40-kW-class SEP provides the necessary capabilities that would enable near term and future architectures, and science missions [5].

Accordingly, NASA has been developing a 13-kW-class Hall thruster EP string that can serve as the building block for a 40-kW-class SEP capability. The 13-kW Hall thruster EP string development, led by the NASA Glenn Research Center (GRC) and the Jet Propulsion Laboratory (JPL), began with the maturation of the high-power Hall thruster and Power Processing Unit (PPU). The technology development and flight qualification work transitioned to Aerojet Rocketdyne via a competitive procurement selection for the AEPS contract in May 2016. Management of the AEPS contract is being led by NASA GRC with funding from NASA's Space Technology Mission Directorate (STMD) under the Technology Demonstration Missions (TDM) program. NASA continues to support the AEPS string development by leveraging in-house expertise, plasma modeling capability, and world-class test facilities.

AEPS Engineering Test Units (ETUs), designed and built by Aerojet Rocketdyne, are undergoing characterization and environmental test campaigns at GRC and JPL [6]. Figure 2 shows a Hall-Effect Rocket with Magnetic Shielding (HERMeS) Technology Development Unit (TDU) next to an AEPS ETU thruster. HERMeS TDU is the high-fidelity precursor to the AEPS ETU. During the development testing of the ETUs, a laser-induced fluorescence (LIF) test was performed. The first objective of the ETU LIF test was to obtain data that can be used to confirm the AEPS ETU exhibits the same ion production and acceleration characteristics as the HERMeS TDU, such that the extensive experimental and modeling works previously performed on the TDU [6-13] are directly applicable to the ETU. The second objective of the test was to measure ion characteristics in the acceleration region, near the pole covers, and in the near-field of ETU thruster to provide data for anchoring plasma models. Of particular interests were any ions that have high energy and can impact the pole covers, such as ions hypothesized to be heated by plasma waves near the chamfer regions [10, 11]. Although not an original objective of the test, data was also obtained at operating conditions
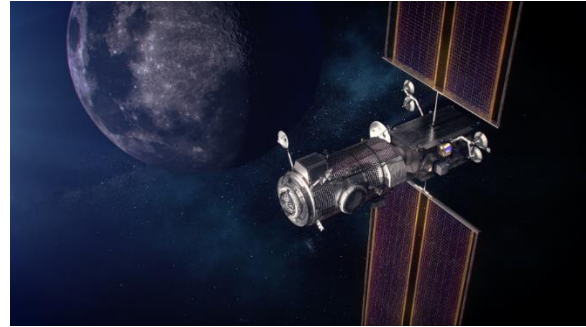
designed to support the PPE mission and the comparison to previously tested operating conditions will be shown in a later paper.

This article will summarize the results of the ETU LIF test and provide comparisons between AEPS ETU and HERMeS TDU. This article will also examine evidence in the measurements related to the existence of the pole-erosion-enhancing plasma waves and provide key characteristics of ions believed to have been energized by said plasma waves.

II. Experimental Setup

To simplify plot labeling, throttle points are labeled by discharge voltage and discharge power. A label that says "300-6.3-B1.00" refers to the throttle point with a discharge voltage of 300 V and a discharge power of 6.3 kW. The value after the letter B indicates multiple of nominal magnetic field strength. For example, "B1.25" indicates 1.25 times the nominal magnetic field strength. If no B value is shown, the B value is 1. Some labels include the background pressure with a unit of "uT" to indicate micro-Torr. Labels without "uT" values indicate the lowest achievable background pressure as described in the Test Facility section. Some labels include "VF5" for Vacuum Facility 5 and "VF6" for Vacuum Facility 6.

A. Thruster and Test Matrix

AEPS ETU data presented in this work were collected with the AEPS ETU2 Hall thruster, manufactured by AR. Figure 3 shows a picture of the AEPS ETU2 installed on the LIF test stand. The AEPS ETU was designed to be a 12.5-kW magnetically shielded Hall thruster with lifetime exceeding 23 kh. The AEPS features a centrally mounted cathode and was designed to be operated with the body electrically tied to the cathode. The AEPS thruster design was derived from the NASA HERMeS TDU to leverage the proven performance and stability of the HERMeS TDU [6]. In addition, AEPS ETU incorporates modifications that improve manufacturability and ability to meet environment and spacecraft interface requirements [14].

During the ETU2 LIF test, the thruster was operated at reference firing conditions (RFCs) ranging from 300 to 600 V, over which the thruster was previously characterized [15, 16]. At all operating conditions, the magnet coils were energized to maintain magnetic shielding topology. Magnetic field strength variation testing was performed in a way that changed the overall magnetic field strength while preserving the field topology. The default cathode flow fraction was 7% for all RFCs except during the cathode flow fraction study. Table 1 shows the thruster RFCs used in the ETU2 LIF test.

B. Test Facility

Testing was performed in Vacuum Facility 5 (VF5) at NASA GRC. This cylindrical facility is 4.6 m in diameter, 18.3 m long, and was evacuated with a set of cryo-pumps. The thruster was mounted on a test stand that can be moved horizontally with two cross-mounted motion stages, as shown in Figure 3. This test stand location was downstream of the test stand location for prior performance and wear tests [15, 16]. Thruster telemetry collected during testing showed that the AEPS ETU2 was operating the same way as in prior testing. Also shown in the figure are the reference target used for laser alignment, the collection optics, and the motion stages.

To accommodate the movement of the thruster during hot-fire, a set of stainless-steel propellant lines were bent to form coils that act as joints, which increased the flexibility of the lines. The propellant lines were then baked out with heat tapes to remove trapped volatiles and ensure high-purity propellant delivery.
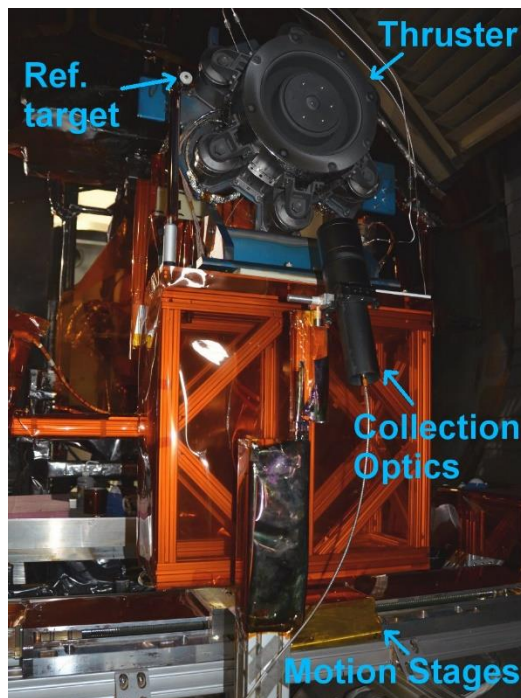

Figure 3. AEPS ETU2 on VF5 LIF test stand.

Table 1. Thruster RFCs for ETU2 LIF test.

Label	Discharge voltage, V	Discharge power, kW
300-6.3	300	6.25
400-8.3	400	8.33
500-10.4	500	10.42
600-12.5	600	12.50

Background pressure near the thruster was monitored with an ion gauge, which was calibrated on xenon against a spinning rotor gauge. Ion gauge readings were corrected for temperature and direction relative to background flux via methods described in Yim and Burt [17]. Uncertainty in the calculated pressure was dominated by plasma-induced noise, electronic noise, and uncertainties associated with correction method. Total uncertainty in pressure measurement was estimated to be 10% to 15% of the reading. At the RFC conditions, the background pressure near the thruster was ~5 micro-Torr. During the background pressure effect study, additional testing was performed at ~12 micro-Torr.

Research-grade xenon propellant was supplied via commercially available mass flow controllers to the anode and cathode. These mass flow controllers were calibrated using research-grade xenon prior to testing. Typical uncertainty of the calibrated measurements were ±1% of reading.

Electrical power was supplied to the thruster with commercially available power supplies. Separate power supplies powered the main discharge, cathode heater, keeper, inner magnet, and outer magnet. An electrical filter was placed between the thruster and the discharge power supply. All power supplies and the filter were located outside of the vacuum facility.

C. Laser Diagnostics and Alignment

The LIF velocimetry scheme used in the ETU2 LIF test excited the XEII 834.953 nm (vac) transition and collected fluorescence from the 542.066 nm (vac) transition [18]. Figure 4 shows a diagram of the spectral transition scheme used. This singly-charged xenon ion transition has an unusually narrow hyperfine structure that cannot be easily resolved even when probed with special techniques [19]. The sigma and pi-polarized Zeeman Effect for this transition was characterized in a prior study [20]. If pi-polarization can be maintained, the broadening in the VDF obtained in the discharge channel of a Hall thruster is at most 4-5% [19]. However, the geometry of the test setup made it impossible to maintain pi-polarization throughout the regions of interest. The decision was made to set the polarization direction of both side injection axes to always be sigma-polarized. The Zeeman-broadened data would then be corrected in post processing using a simplified linear model developed by Huang in a prior work [20]. The axial injection axis was set to allow pi-polarization throughout most of the discharge channel while accepting increased broadening in certain regions. Within these regions, only the VDF width data from the side injection axes were used.

The laser used in this LIF test was a taper-amplified diode laser that can output up to 500 mW at 835 nm. Wavelength was monitored via a Fizeau-type wavemeter and periodically checked with an optogalvanic cell. The laser beam was also monitored with a photodiode to track the variation in laser power. This was found to vary by less than 2% in any given scan. The laser beam was split into three branches. Each branch passed through an electro-optical modulator and was collimated into an optical fiber. A modulation frequency study showed that the signal-to-noise ratio (SNR) optimized at around 300 kHz to 350 kHz. An improvement was made in this LIF setup compared to the one used for the TDU1 LIF test in VF6 [7]. Quarter-wave-plates were used to maximize the extinction ratio of the electro-optical modulator in this LIF setup that corresponded to an improvement in SNR of a factor of ~2.

Figure 5 shows a diagram of the optics setup inside the vacuum facility. Part (a) of the figure shows the three sets of injection optics that were deployed. The optical fibers from the air-side setup were sent to each of the three sets of injection optics. Each set of injection optics had two motors that allowed remote control of the tilt and pan. The optics on axis 1, the axial axis, was protected from most of the heat of the plasma by a shield. Additionally, the support structure for the axis 1 optics was equipped with an internal cooling line connected to a chiller. The thruster was mounted on the motion stages that provide radial and axial movements. A reference target was mounted at a known distance from the thruster in the same plane as the three injected laser beams. Two cameras monitored the positions of the injected laser beams relative to the reference target. Part (b) of the figure shows the collection optics that were mounted 70° out of the injection plane. An optical fiber carried fluorescence signal from the collection optics out of the vacuum facility. The characteristic spatial resolution of approximately 1 mm in size was limited by the beam waist of the injection beams and the viewing cone of the collection optics.

The light from the collection optical fiber was filtered by a monochromator and sent to a photomultiplier. The photomultiplier current was converted to voltage via a high-speed trans-impedance amplifier. The output voltage signal was coupled into three digital lock-in amplifiers. A computer controlled the movement of various stages, swept the laser wavelength, and recorded the various output signals. Lock-in amplifier time constant varied from 300 ms to 1 s.
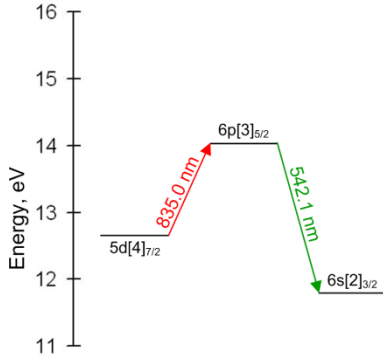
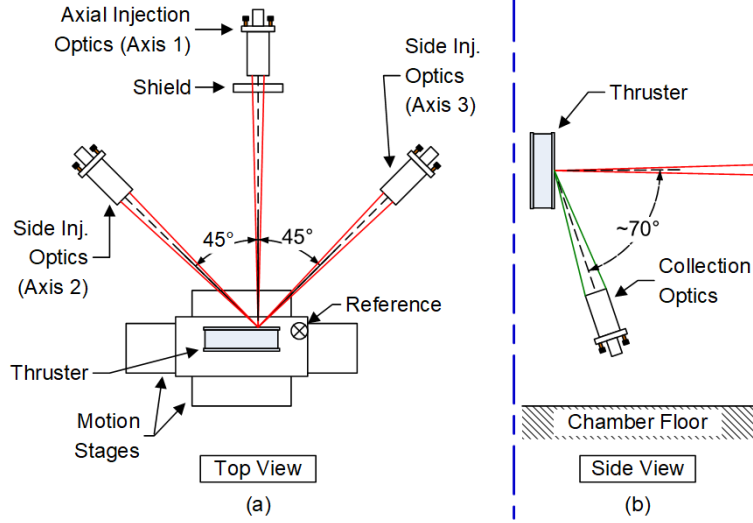**Figure 4. Transition diagram for Xe II LIF at 834.953 nm (vac).**

Figure 5. Vacuum-side optical setup.

Due to the small size of the interrogation zone relative to the length scale of the rest of the vacuum facility, shifts in laser alignment over the course of the experiment can take the injected beams and the collection optics out of alignment if not corrected for. The LIF system used a reference pin, an image disc, and two cameras to track the position of the laser beams relative to the thruster. Since the reference pin was 1 mm in diameter, change in alignment as small as 0.1 mm could be detected by measuring the intensity of the laser light reflected off of the alignment pin. If the alignment of a laser beam drifted by more than 1 mm and the image fell on the image disc, it was detected via the cameras and brought back into alignment.

III.   Data Analysis

A. Analysis Method

A saturation study was performed at the beginning of the test campaign to set the injection laser power to maintain an acceptable level of broadening while maximizing the SNR (i.e. high laser intensity leads to higher SNR but also more saturation broadening). In the discharge channel, the amount of broadening was up to 5% except at the farthest upstream position where broadening was up to 15%. VDF width data from the farthest upstream position will not be reported. Near the pole covers where the VDFs tended to be broader than in the discharge channel, the neutral filter was decreased by 0.1 and the amount of broadening was up to 6%.

The first step in the data analysis was to convert the wavemeter readings into frequency shift relative to the stationary transition frequency. This frequency shift was then converted into a velocity scale.

The change in laser power was assessed with a combination of photodiode and thermopile prior to test and monitored with the same photodiode during test. Due to the laser power varying by less than 2% throughout each laser scan, no correction for laser power was made to the data.

Next, curve-fits were performed on plots of intensity versus velocity. Three curve-fits form were used. Eqs. (1), (2), and (3) shows the mathematical forms of the skew-normal, Gaussian, and two-Gaussian fit functions, respectively.

$$I = c_1 e^{-\frac{(v-c_3)^2}{2c_2^2}} \left\{ 1 + erf\left[\frac{c_4(v - c_3)}{\sqrt{2}c_2}\right]\right\} \tag{1}$$

$$I = c_1 e^{-\frac{(v-c_3)^2}{2c_2^2}} \tag{2}$$

$$I = c_1 e^{-\frac{(v-c_3)^2}{2c_2^2}} + c_4 e^{-\frac{(v-c_6)^2}{2c_5^2}} \tag{3}$$

Where I is the intensity, v is the velocity, c_1 to c_6 are curve-fit constants, and erf is the error function. Figure 6 shows an example of skew-normal curve-fit. Figure 7 shows an example of two-Gaussian curve-fit. The analysis program could also export the remainder data after each curve-fit was applied so that the remainder could be curve-fitted in case there were more than two peaks in the data.

A set of rules were developed and applied for all curve-fitting. These rules were set for specific locations because the characteristics of the ion VDFs were highly location dependent.

For the data sets located radially between the outer edge of the inner front pole cover (IFPC) and the inner edge of the outer front pole cover (OFPC), the process began with the application of skew-normal curve-fit to every location. The resulting averaged velocity was calculated to map out the rough location of the acceleration zone. Here, the acceleration zone was defined as the region where the magnitude of averaged ion velocity was between 10% and 90% of the maximum magnitude of the ion velocity reached. For any locations within or downstream of the acceleration zone, a two-Gaussian fit was applied if either one of two criteria were met. Criterion one was if the coefficient of determination (a.k.a. R squared), a measure of the goodness of the fit, falls below 0.9. Criterion two was if the user found, in visual inspection, a saddle point in the data. Here a saddle point was defined as a section of data with positive concavity sandwiched by two sections of data with negative concavity. Mathematically, the concavity of a graph is its second derivative. Figure 8 illustrates the definition of the saddle point. In this figure, the vertical dashed gray lines indicate where the concavity changes sign and the gray arrows indicate the direction of concavity (a down arrow represents negative concavity and vice versa). Once the two-Gaussian fit was applied, the second derivative of the resulting curve-fit was examined for the presence of a saddle point. This second examination provided an important confirmation to the presence of the saddle point because there might not have been in initial examination (if criterion one was invoked) or the initial examination of the data with noise might have only given the user an illusion of a saddle point. If no saddle point was found or the R squared value of the two-Gaussian fit was lower than that of the skew-normal fit, the skew-normal fit was accepted. Otherwise, the two-Gaussian fit was accepted. Note that the application of the two-Gaussian fit was triggered by the criteria being met on either axes 2 or 3 but the resulting two-Gaussian fit was not accepted unless saddle points were found on both axes 2 and 3 and the R squared values of the two-Gaussian fits were found to be higher on both axes. Axis 1 data was used to help interpret the physical meaning of the data, as will be explained later in the article.

For data sets located near the IFPC, both skew-normal and two-Gaussian curve-fits were applied and the saddle point and R square criteria were used to determine which curve-fit should be accepted. For data sets located near the OFPC, data was not found to contain two ion populations per the saddle point and R square criteria. Furthermore, SNR of data near OFPC was generally low and the Gaussian fit was used instead of the skew-normal fit when the SNR was less than 4. When the SNR was less than 4, the skew-normal fit sometimes fitted a long tail in either the positive or negative direction the magnitude of which was below the magnitude of the noise. Such a tail was typically statistically insignificant (magnitude of tail less than two times the standard deviation of the noise). In such a case, using the Gaussian fit guaranteed that subsequent calculations only used the part of the data that was statistically significant. However, ion VDFs in Hall thruster plasma tended to have tails, which is why the process defaulted to skew-normal except when the SNR was low.

If additional structures remain in the data after subtracting the curve-fit, additional curve-fit to remainder data can be applied. For this paper, this was the main method by which the third ion population near the IFPC was identified. SNR for any third peak found was separately assessed for statistical significance.

For the side injection axis, which were purely sigma-polarized, Zeeman Effect on the hyperfine structure was corrected by applying a simple linear model for the XEII 834.953 nm (vac) transition [20]. The model is reproduced here in the form of Eq. (4) for convenience.
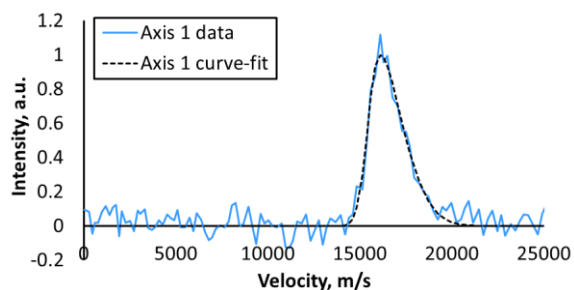

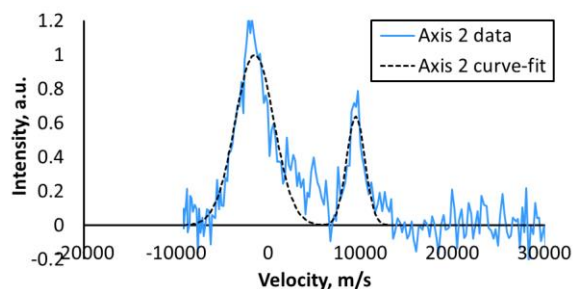**Figure 6. An example of skew-normal curve-fit.**

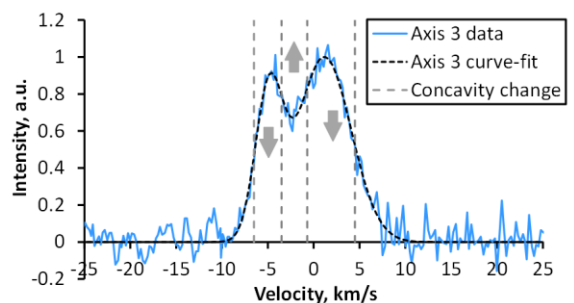**Figure 7. An example of two-Gaussian curve-fit.**

Figure 8. An illustration of a saddle point that hints at the existence of two Gaussian peaks.

$$Zeeman\ splitting\ in\ MHz = 2.7273 \times Magnetic\ field\ strength\ in\ Gauss \qquad (4)$$

Magnetic field strength values from a simulation of the ETU was used with the above model. This magnetic field simulation was validated using measurements of the ETUs. At each location where LIF data was taken, the magnetic field strength in the axial-radial plane was extracted from the simulation and inputted into Eq. (4). The resulting splitting amount was convoluted with the curve-fit and then compared to the line shape. Once a set of acceptable curve-fit parameters were obtained, the curve-fit without the Zeeman Effect was calculated. On average, the Zeeman Effect correction reduced the width of the VDFs by about 2-6%. However, in regions of high magnetic field, the correction reduced the width of the VDFs by as much as 40%.

Once the curve-fits with Zeeman Effect corrections were performed, averaged velocities and full-width-at-half-maximum (FWHM) velocities were calculated. If a two-Gaussian fit was accepted as the best fit, the averaged and FWHM velocities were calculated differently depending on the location associated with the data. For data found in the acceleration zone of the thruster, plasma oscillation is known to spread out time-averaged VDFs in such a way as to show two peaks; in this zone, the two-Gaussian fits were analyzed as if they were a single population [21]. For these cases, the vector angles of the two peaks were checked to see if they were within 10° of each other (i.e. moving in the same direction but spread out by plasma oscillations). For data found near the discharge channel but downstream of the acceleration zone, the two peaks found were assumed to be two distinct populations. In such a case, the averaged energy and direction of the two peaks were separately calculated.

For the ion populations of interest, such as when two or more peaks were found near the inner front pole or a single peak found near the outer front pole, analyses were performed using the Monte Carlo method to construct the ion energy distribution function (IEDF) of each population from axes 2 and 3 curve-fit results. An assumption is made that for each ion population the associated axes 2 and 3 VDFs are randomly correlated. From that assumption, 10,000 ion particles were simulated from each pair of axes 2 and 3 VDFs and the resulting particle energies were binned to generate probability histograms. The averaged energy and FWHM energy were calculated from the constructed IEDF. Percentage of the population with energy in excess of a threshold energy of 50 eV was also calculated. This threshold value was picked based on the approximate value above which graphite sputter yield starts to become non-trivial in literature survey [22]. This parameter provided a rough measure of the percentage of erosive ions present in the IEDF. Figure 9 shows an example of the IEDF construction. In this figure, the vertical black dashed line indicates the averaged energy, the horizontal black dashed line indicates the FWHM energy, and the red solid curve indicates the fitting of a drifting Maxwellian distribution with isotropic temperatures for visual reference.
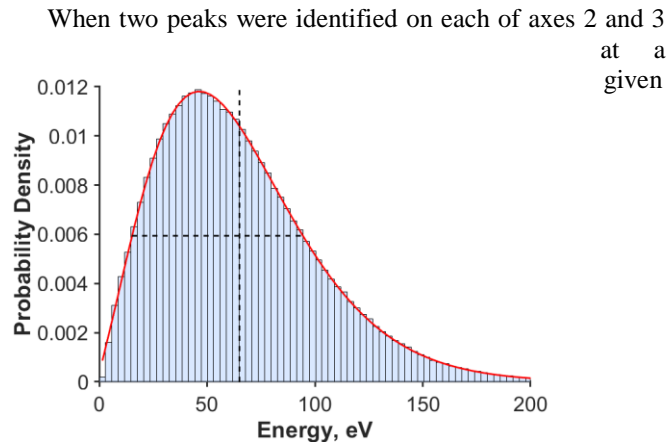
When two peaks were identified on each of axes 2 and 3 at a given

Figure 9. An example of reconstructing the ion energy distribution function from velocity distribution functions on two axes.
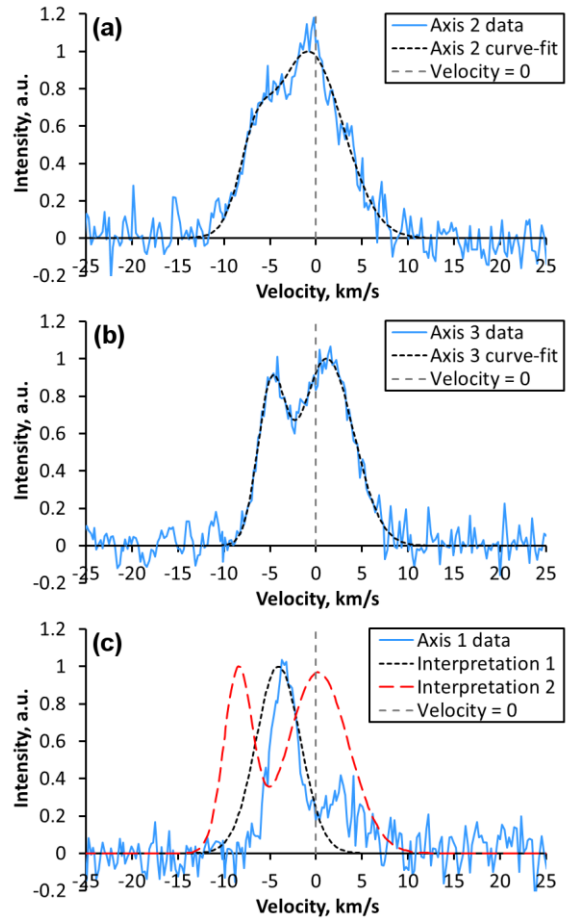

Figure 10. Examples of two-peak structures found near the IFPC on (a) axis 2, (b) axis 3. (c) shows axis 1 data overlaid with two different interpretations of axes 2 and 3 data.

location, an analysis was performed to determine how the two peaks correlate. Figure 10 shows an example of LIF data with two peaks on each of axes 2 and 3. In one interpretation of the data, the left peak on axis 2 correlates with the left peak on axis 3; in another interpretation, the left peak on axis 2 correlates with the right peak on axis 3. These interpretations can be used to predict the appearance of the axis 1 (axial axis) VDF. Figure 10(c) shows an example of the two interpretations overlaid on top of the example axis 1 data. For ETU2 LIF test data, it was the case that at any given location one of the interpretations would provide a much better agreement with the data than the other interpretation. This analysis showed that, as was the case with TDU in VF6 [7], there were at least two streams of ions moving in opposite directions across the IFPC of the ETU2. Using a similar method, it was possible to isolate a third ion population that was also moving across the IFPC of the ETU2.

B. Uncertainty Analysis

The uncertainty in position was dominated by the size of the interrogation zone and the drift in alignment of the optics. The alignment procedure used in this LIF test rejected data where alignment drifted by more than 0.5 mm from the reference.

The SNR, defined as the ratio of the peak signal divided by the standard deviation of the noise, was an important metric in assessing uncertainty in the data. Typically, any trace with an SNR of 2.5 or less was considered statistically insignificant. At this value of SNR, any peak present was barely detectable against the noise. Since three injection axes were used, if the SNR was low on one axis, a velocity vector could still be calculated from the remaining two axes. Where reliable data was available from all three axes, calculations of the axial velocity were performed using different combination of axes to assess the uncertainties in the calculated velocities. Additionally, the uncertainty from the wavemeter was estimated at ±50 m/s. Scanning resolution of the laser was set sufficiently fine so as not to contribute to the total uncertainty. Combining all sources of uncertainty via standard error propagation, the effective total uncertainty was ±112 m/s for measurements in the discharge channel, ±700 m/s near the pole covers, and ±900 m/s for non-beam-energy populations found near the chamfer.

IV. Results

Unless otherwise noted, all spatial positions around the thruster are normalized based on the region of interest. For the thruster discharge channel, radial positions are normalized by the discharge channel width, where R = 0 is the inner wall, R = 1 is the outer wall, Z = 0 is the exit plane as defined by the inner front pole cover downstream surface, and Z is positive in the downstream direction. Similarly, data near the inner and outer front pole covers are normalized so that R = 0 and R = 1 correspond to the inner and outer radial edges, respectively, of the region of interest.

A. Identification of the third ion population near the IFPC

Compared with a previous LIF study on the TDU1 [7], where two counter-streaming ion populations were identified near the IFPC, a third ion population was identified in this study. Figure 11 shows example data from a location near the ETU2 IFPC (R = 0.76, Z = 0.08). The blue solid and dashed curves show the data and curve-fit, respectively, from the 600 V, 12 kW condition, where only two peaks were identified on each of axes 2 and 3 and only one peak on axis 1 due to overlap (See Figure 10 for an illustration of why these two peaks overlap on axis 1). The orange solid and dashed curves show the data and curve-fit, respectively, from the 300 V, 3 kW condition, where an additional peak was identified on all three axes. The correlation technique described in the Analysis Method section was used and the extra peak on the three axes correlates well with each other.

Notably, this third IFPC ion population was only detectable for 300 V operating conditions. Whereas this population could be clearly identified across the IFPC for the 300 V, 3 kW condition, it became harder to identify (lower SNR) as the thruster goes to higher-power 300 V operating condition. For the 400 V operating condition, small bumps in the data could be found where this population should be located but the SNR was too low for statistical significance. For 500 V and 600 V operating conditions, the third IFPC ion population could not be located. The key characteristic of this ion population appears to be that it has much higher energy than the other IFPC populations (100-150 eV) but lower than the energy of the main beam. This third population also closely match the characteristics of the single OFPC population except that the velocity vectors were pointed in the opposite direction (radially inward). It should be noted that the single OFPC population was easily detectable at all 300 V condition but was often difficult to detect for higher voltage operations (i.e. low SNR). For the purpose of this paper, the third IFPC population is referred to as the medium-energy population to separate it from the low-energy and beam-energy ion populations. Further descriptions of this medium-energy population will presented in the following sections.

B. ETU to TDU comparison – Facility and background pressure effects

To examine the similarity in the ion production and acceleration characteristics between the AEPS ETU and the HERMeS TDU several comparisons were made of the LIF data as different parameters were varied. Figure 12 shows the averaged axial velocity of the ions along discharge channel centerline for both ETU and TDU in different test facilities while the thruster operated at the 300 V, 6.3 kW condition.

Figure 11. Example data and curve-fits for (a) axis 1, (b) axis 2, and (c) axis 3 the when a third peak is present (orange) versus when it is not (blue).

Note that the background pressure near the thruster is also shown in the figure. Figure 13 shows the same for operations at 600 V, 12.5 kW. The data set labeled "TDU1, VF6" is described in [7, 13], the data set labeled "Owens 2016" is described in [23], and the data set labeled "Owens 2018" is described in [24].
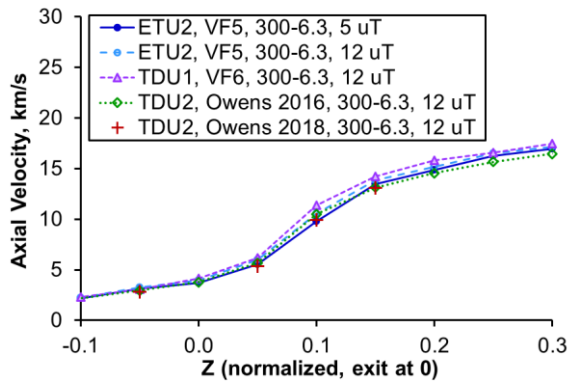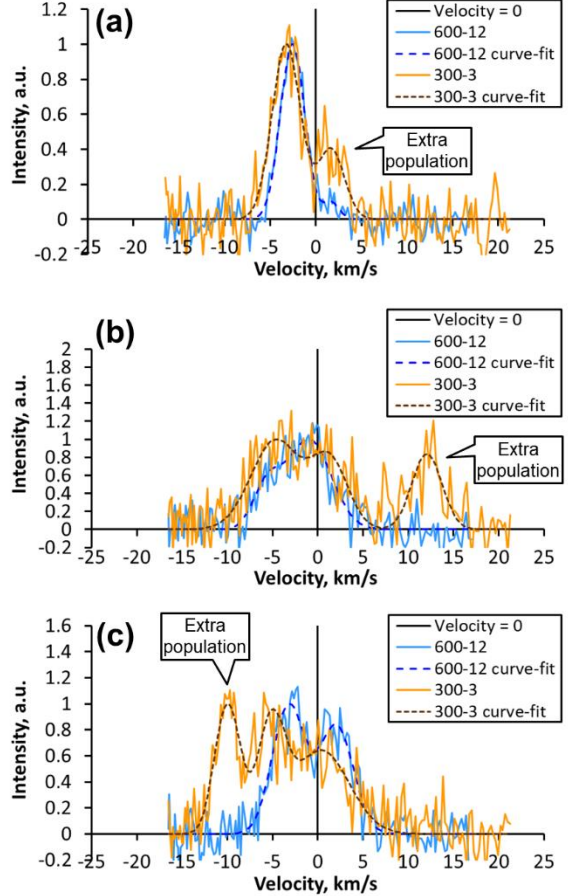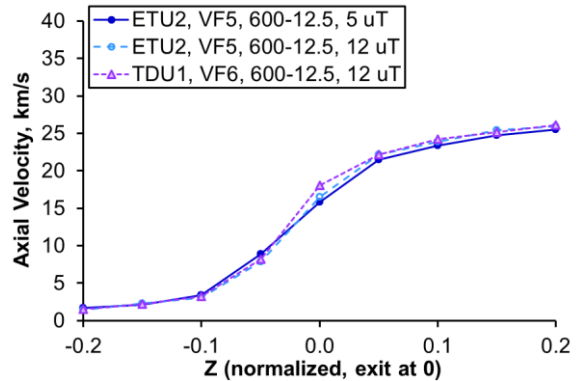

Figure 12. Averaged axial ion velocity along discharge channel centerline for several ETU and TDU LIF studies with thruster at 300 V, 6.3 kW.

Figure 13. Averaged axial ion velocity along discharge channel centerline for several ETU and TDU LIF studies with thruster at 600 V, 12.5 kW.

From the above figures, one can see that the difference in behavior between the test facility is very small. For 300 V, 6.3 kW operations, when ETU2 was operated in 12 micro-Torr background pressure in VF5 to match the lowest

achievable background pressure in VF6 and Owens chamber, the difference in the acceleration profile was statistically insignificant. When ETU2 was operated in the lowest achievable background pressure of 5 micro-Torr in VF5, the difference between ETU2 and TDUs became statistically significant but still very small. Similarly, only small differences were observed between test facilities when operating at 600 V, 12.5 kW.

Figure 14 shows a comparison of the results from the ETU2 background pressure study in VF5 alongside TDU1 background pressure study at the same operating condition of 300 V, 6.3 kW in VF6. In both tests, the acceleration zone moved upstream with increasing background pressure. The movement of ~0.01 over a change of 7 micro-Torr for ETU2 in VF5 was very similar to the movement of ~0.018 over a change of 10 micro-Torr for TDU1 in VF6, implying that similar physics was at work.

Figure 15 shows the averaged ion velocity vector plot in the axial-radial plane for the discharge channel region of ETU2 while operating at 300 V, 6.3 kW in 12 micro-Torr background pressure inside VF5. Figure 16 shows the same for TDU1 inside VF6. In these figures (and subsequent discharge channel velocity vector plots), the black arrow represents populations that had been identified as beam ions.

Figure 14. Averaged axial ion velocity along discharge channel centerline for ETU2 and TDU1 at 300 V, 6.3 kW and various background pressures.

They tended to reach energy closer to the discharge voltage, have narrow (~50 eV) FWHM energy once past the acceleration zone and have high peak height relative to other observed ion populations. The acceleration zone can be seen in the averaged velocity vector plots of the discharge channel visually as the locations where the length of the black arrows grow rapidly as one travels downstream. Also, in these discharge channel velocity vector plots, low and medium energy ion populations (non-beam-energy populations) are identified with green arrows for ETU and blue arrows for TDU.
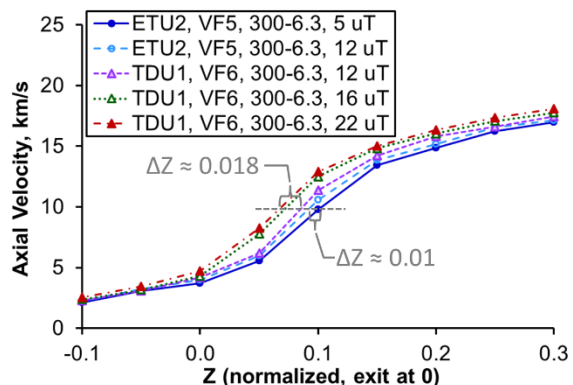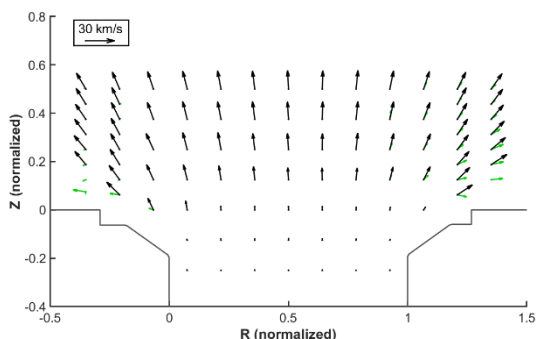

Figure 15. Averaged velocity vector in the discharge channel for ETU2 operating at 300 V, 6.3 kW in VF5 at 12 micro-Torr background pressure.
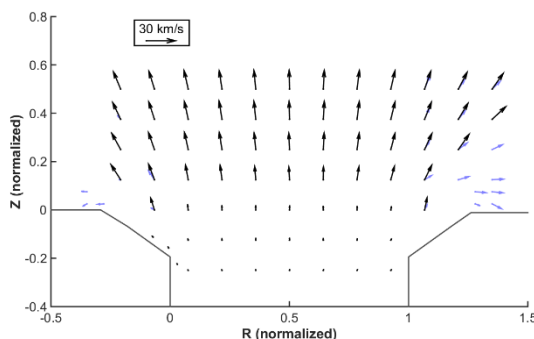

Figure 16. Averaged velocity vector in the discharge channel for TDU1 operating at 300 V, 6.3 kW in VF6 at 12 micro-Torr background pressure.
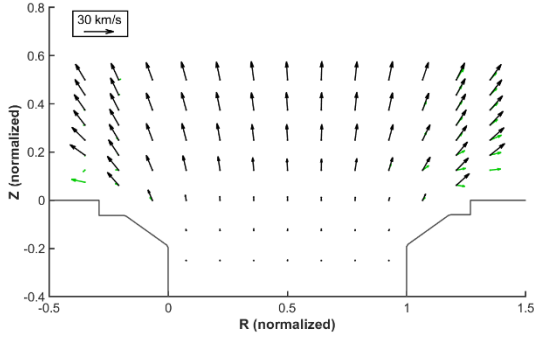
Figure 17. Averaged velocity vector in the discharge channel for ETU2 operating at 300 V, 6.3 kW in VF5 at 5 micro-Torr background pressure.

From Figures 15 and 16, one can see that the beam ions have very similar averaged velocity vectors. From here on, when describing discharge channel velocity vector plots, regions of the discharge channel radially between the inner and outer channel walls will be referred to as the main beam region. The regions radially inward and outward from the main beam region will be referred to as the inner and outer beam edge regions, respectively. Near-chamfer region refers to the region downstream of the chamfer down to roughly Z = 0.3 or so. An examination of the velocity values shows that for the main beam region, the difference in axial and radial velocities between ETU2 in VF5 and TDU1 in VF6 were up to 800 m/s for the 300 V, 6.3 kW condition (and up to 1800 m/s for the 600 V, 12.5 kW condition). The differences in the beam edge region were up to 1300 m/s for the 300 V, 6.3 kW condition, and up to 800 m/s for the 600 V, 12.5 kW condition. The differences tended to be higher towards the radial edges of the beam (left and right extremes in Figures 15 and 16) where ion density tended to be low and SNR was correspondingly low. Given the good match in velocity vector in the main beam region and most of the beam edge regions, effect of different test facility and ETU versus TDU appears to be small. Note that a portion of the differences measured in the velocity vector between ETU2 in VF5 and TDU1 in VF6 in the beam edge regions were statistically significant, but their values were small enough such that they were considered unimportant as long as there were no statistically significant difference in the data at the neighboring pole cover locations.

Figure 17 shows the discharge channel averaged ion velocity vector for ETU2 operating at 300 V, 6.3 kW in VF5 at 5 micro-Torr background pressure. An examination of the velocity values shows that the differences between ETU2 operating in 5 versus 12 micro-Torr was up to 800 m/s in the main beam region, up to 4 km/s in the inner beam edge region, and up to 2.2 km/s in the outer beam edge region. The largest differences were located near the beam edges, close to the chamfers. While the differences are not very large (compared to the 20 km/s that the beam ions reached), they could have some implications for pole erosion and closer examination of the pole cover data will be performed next. Note that data acquisition domain did not extend as far into the beam edge for the 600 V, 12.5 kW study. The trends in the data were very similar for 600 V, 12.5 kW condition in the regions where data was acquired.

Figures 18 and 19 show the averaged ion velocity vector near the IFPC and OFPC, respectively, of the ETU2 operating at 300 V, 6.3 kW in VF5 at 5 micro-Torr background pressure. Figures 20 and 21 show the same for ETU2 in VF5 at 12 micro-Torr background pressure. Figures 22 and 23 show the same for TDU1 in VF6 at 12 micro-Torr background pressure. Note that velocity scale for Figure 22 is different than for the other two IFPC plots shown. In the IFPC vector plots, a black arrow indicates a location where only one peak could be definitively identified, a red arrow indicates a low-energy ion population coming from the discharge channel and a blue arrow indicates a low-energy ion population coming from the cathode. A green arrow indicates a medium-energy ion population coming from the discharge channel. It was possible that some black arrows were average of two (maybe three) ion populations that overlapped enough to be impossible to separate when curve-fitting. Note that the TDU1 data was from a prior test [7] and no attempts had yet been made to identify whether the third IFPC population (green arrow) exist.

To better quantify the global trends in the data, the ion characteristics for the facility and background pressure studies were averaged and tabulated. Table 2 summarizes the averaged ion energy, FWHM energy, percentage of population with more than 50 eV, and averaged angle-of-incidence (AOI) with respect to the IFPC surface normal for the low-energy stream from the discharge channel and the stream from the cathode. An AOI value of 0° corresponds to the ions coming into the pole cover at normal incidence. An AOI value of 90° corresponds to grazing incidence. For this table, the averaging was performed over all IFPC locations except the innermost and outermost locations seen in the IFPC plot. At the innermost radial locations, typically only cathode ions were detected. At the outermost radial locations, for some conditions, overlapping ion populations were detected and the populations could not be clearly separated. For Table 2, sample size was at least 10 for every condition and was not individually listed. Note that it was shown in a previous study that LIF data locations near the pole were outside of the plasma sheath [13] and, for the ETU2, the sheath voltage drop was estimated to be the same as the TDU1 at 20-30 eV. Table 3 summarizes the same parameters for the third ion population (medium-energy) found near the IFPC. Note that the number of samples (listed in the table) were limited as the third ion population was often difficult to detect over the other two IFPC ion populations. Also, the AOI listed are slightly greater than 90°, which means that on average these ions do not impact the IFPC. However, these ions have a spread and it is expected that a small fraction of them could reach the pole cover.

Further analysis will be performed in the future to estimate this fraction. Table 4 summarizes the same for the single ion population found near the OFPC. For this table, the averaging was performed over all OFPC locations where peaks were statistically significant. Number of samples averaged for each condition was listed. For 600 V, 12.5 kW operations, data was only statically significant at 1 to 3 locations per condition, there was not enough samples to make statistically meaningfully comparisons.
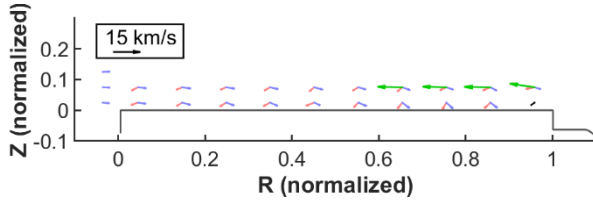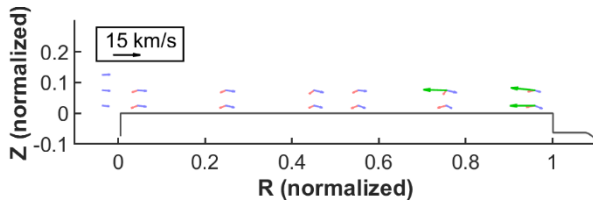

Figure 18. Averaged velocity vector near the IFPC for ETU2 operating at 300 V, 6.3 kW in VF5 at 5 micro-Torr background pressure.
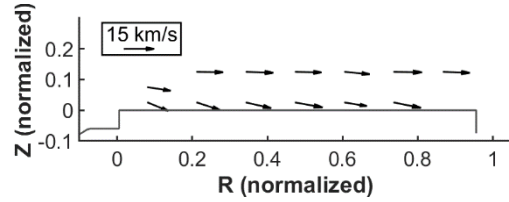
Figure 19. Averaged velocity vector near the OFPC for ETU2 operating at 300 V, 6.3 kW in VF5 at 5 micro-Torr background pressure
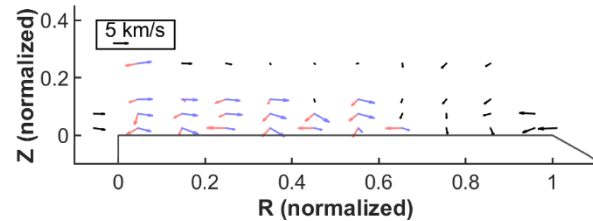

Figure 20. Averaged velocity vector near the IFPC for ETU2 operating at 300 V, 6.3 kW in VF5 at 12 micro-Torr background pressure.
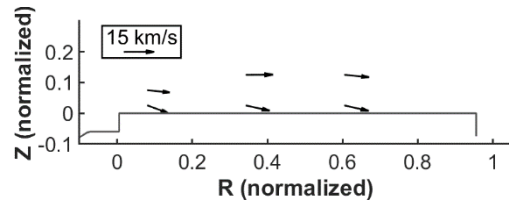
Figure 21. Averaged velocity vector near the OFPC for ETU2 operating at 300 V, 6.3 kW in VF5 at 12 micro-Torr background pressure.

Figure 22. Averaged velocity vector near the IFPC for TDU1 operating at 300 V, 6.3 kW in VF6 at 12 micro-Torr background pressure.
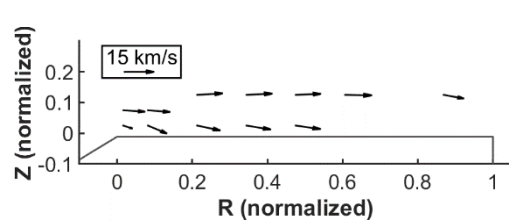

Figure 23. Averaged velocity vector near the OFPC for TDU1 operating at 300 V, 6.3 kW in VF6 at 12 micro-Torr background pressure.

Table 2. IFPC ion characteristics for the facility and background pressure studies.

Thruster	Condition	Facility	Pressure, uT	Discharge Channel Low-Energy Stream				Cathode Stream			
				E_{AVG}, eV	E_{FWHM}, eV	% above 50 eV	AOI_{AVG}, degree	E_{AVG}, eV	E_{FWHM}, eV	% above 50 eV	AOI_{AVG}, degree
ETU2	300-6.3	VF5	5	22	25	4.1	48	26	32	8.8	63
ETU2	300-6.3	VF5	12	19	24	3.3	57	25	31	8.4	73
TDU1	300-6.3	VF6	12	24	21	6.5	48	30	32	15.5	66
ETU2	600-12.5	VF5	5	19	23	2.3	53	25	32	8.5	65
ETU2	600-12.5	VF5	12	18	20	1.0	46	27	34	10.1	67
TDU1	600-12.5	VF6	12	22	23	3.7	43	27	29	10.2	61

Table 3. Third IFPC ion characteristics for the facility and background pressure studies

Thruster	Condition	Facility	Pressure, uT	Sample Size	E_{AVG}, eV	E_{FWHM}, eV	% above 50 eV	AOI_{AVG}, degree
ETU2	300-6.3	VF5	5	4	145	96	99.6	94
ETU2	300-6.3	VF5	12	3	129	79	99.8	93

Table 4. OFPC ion characteristics for the facility and background pressure studies

Thruster	Condition	Facility	Pressure, uT	Sample Size	E_{AVG}, eV	E_{FWHM}, eV	% above 50 eV	AOI_{AVG}, degree
ETU2	300-6.3	VF5	5	11	119	90	96.8	80
ETU2	300-6.3	VF5	12	5	108	86	93.9	79
TDU1	300-6.3	VF6	12	8	119	77	98.4	84

Comparing Figures 22 and 23 to Figures 20 and 21, one can see that the ion vectors were very similar between the ETU2 in VF5 and TDU1 in VF6 at the same background pressure. Examination of Table 2 shows that for the 300 V, 6.3 kW condition, the cathode stream was slightly more energetic for the TDU1 in VF6 than for the ETU2 in VF5. Differences in the discharge channel low-energy stream and for the 600 V, 12.5 kW condition were small enough to be not statistically significant. Examination of Table 4 shows that the OFPC ions had very similar characteristics.

Comparing Figures 18 and 19 to Figures 20 and 21, one can see the ion vectors were very similar between ETU2 in VF5 in 5 versus 12 micro-Torr background pressure. The values shown in Table 2 and Table 4 are also nearly identical. On the other hand, Table 3 appears to show that the energy (both averaged and FWHM) of the third IFPC ion population decreases with increasing background pressure. At this point, there was not enough information to be able to determine whether the third IFPC population was a major contributor to pole erosion but its trend with background pressure is noteworthy and will be discussed further in a later section.

C. ETU to TDU comparison – Magnetic variation

Figure 24 and Figure 25 show the averaged axial velocity of the ions along discharge channel centerline for ETU2 operating at the 300 V, 6.3 kW and 600 V, 12.5 kW conditions, respectively, and different magnetic field strength. As was the case with TDU1 [25], the acceleration zone of the ETU2 moved upstream with increasing magnetic field strength. This trend was prominent for operations at 300 V discharge but much less prominent for operations at 600 V.
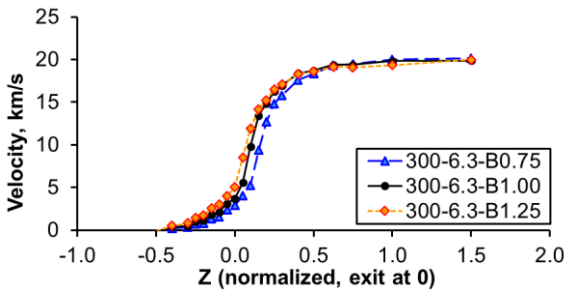
Figure 24. Averaged axial ion velocity along discharge channel centerline for ETU2 at 300 V, 6.3 kW and different magnetic field strength.
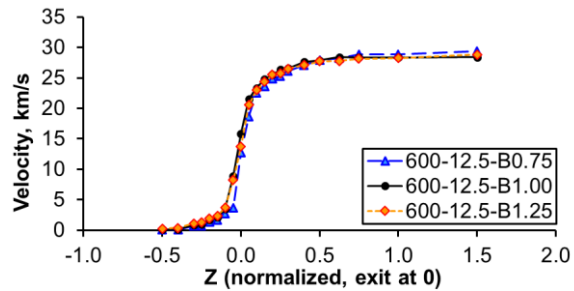
Figure 25. Averaged axial ion velocity along discharge channel centerline for ETU2 at 600 V, 12.5 kW and different magnetic field strength.

Similar to the facility and background pressure study, the discharge channel velocity vectors were compared between the ETU2 in VF5 and TDU1 in VF6. Except for a few near-chamfer locations the velocity vectors were nearly identical between the two data sets showing that the ETU behaved like the TDU.

Figures 26 and 27 show the averaged ion velocity vector near the IFPC and OFPC, respectively, of the ETU2 operating at 300 V, 6.3 kW, and 0.75 times nominal magnetic field strength. The blue arrow in Figure 27 was likely a small amount of beam ions that could be detected at that location. Figures 28 and 29 show the same type of plots for the thruster operating at 1.25 times nominal magnetic field strength. The medium-energy ion population found near the IFPC could not be definitively identified for the 0.75 times field strength condition but was successfully identified for the 1.25 times field strength condition.

Table 5 summarizes the energy and angle characteristics of the low-energy stream from the discharge channel and the stream from the cathode for the magnetic variation study. Averaging was performed over the same IFPC locations as for Table 2. Table 6 and Table 7 summarize the same parameters for the medium-energy population from the discharge channel arriving at the IFPC and OFPC, respectively.
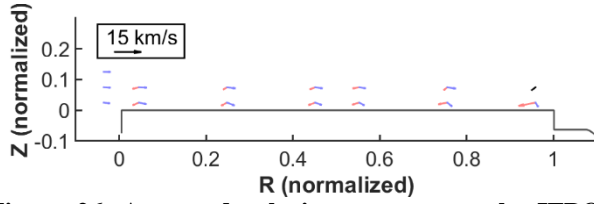

Figure 26. Averaged velocity vector near the IFPC for ETU2 operating at 300 V, 6.3 kW, 0.75x nominal magnetic field strength.
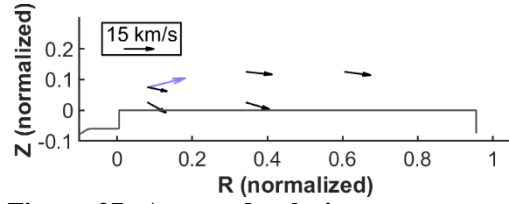
Figure 27. Averaged velocity vector near the OFPC for ETU2 operating at 300 V, 6.3 kW, 0.75x nominal magnetic field strength.
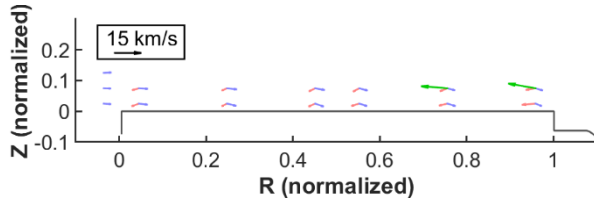
Figure 28. Averaged velocity vector near the IFPC for ETU2 operating at 300 V, 6.3 kW, 1.25x nominal magnetic field strength.
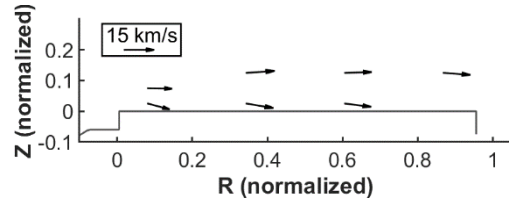

Figure 29. Averaged velocity vector near the OFPC for ETU2 operating at 300 V, 6.3 kW, 1.25x nominal magnetic field strength.

Table 5. IFPC ion characteristics for the ETU2 magnetic variation studies.

		Discharge Channel Low-Energy Stream				Cathode Stream			
Condition	Sample Size	E_{AVG}, eV	E_{FWHM}, eV	% above 50 eV	AOI_{AVG}, degree	E_{AVG}, eV	E_{FWHM}, eV	% above 50 eV	AOI_{AVG}, degree
300-6.3-B0.75	10	18	21	2.9	62	20	26	4.5	69
300-6.3-B1.00	18	22	25	4.1	48	26	32	8.8	63
300-6.3-B1.25	10	21	28	6.5	61	26	35	10.1	73
600-12.5-B0.75	10	14	18	0.3	44	20	27	3.5	64
600-12.5-B1.00	18	19	23	2.3	53	25	32	8.5	65
600-12.5-B1.25	10	21	27	5.9	55	28	38	12.2	69

Table 6. Third IFPC ion characteristics for the ETU2 magnetic variation studies

Condition	Sample Size	E_{AVG}, eV	E_{FWHM}, eV	% above 50 eV	AOI_{AVG}, degree
300-6.3-B1.00	4	145	96	99.6	94
300-6.3-B1.25	3	170	110	100.0	100

Table 7. OFPC ion characteristics for the ETU2 magnetic variation studies

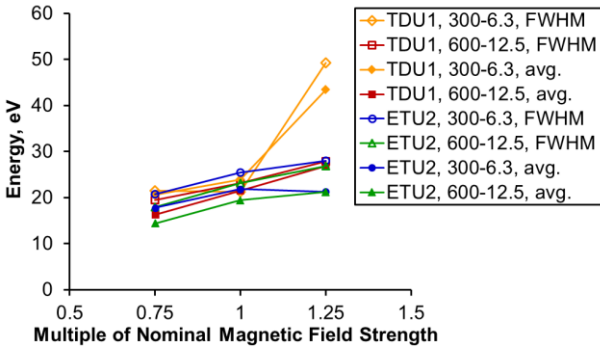| Condition	Sample Size	E_{AVG}, eV	E_{FWHM}, eV	% above 50 eV	AOI_{AVG}, degree
300-6.3-B0.75	4	126	110	91.9	78
300-6.3-B1.00	11	119	90	96.8	79
300-6.3-B1.25	6	127	97	97.2	85

Figure 30. Trends in energies of the discharge channel low-energy stream with magnetic field strength for the ETU2.
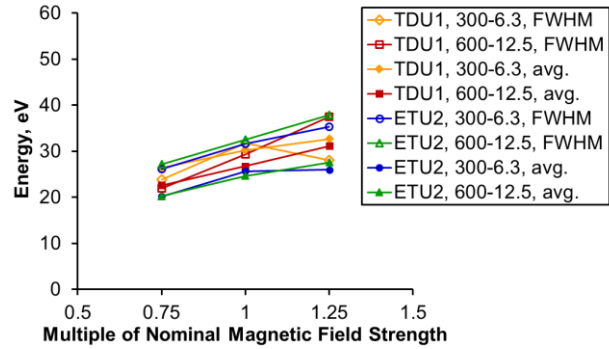
Figure 31. Trends in energies of the cathode stream with magnetic field strength for the ETU2.

Figure 30 and Figure 31 shows how the energy (averaged and FWHM) of the discharge channel low-energy stream and the cathode stream, respectively, trends with magnetic field strength for both the ETU2 in VF5 and TDU1 in VF6 [7]. Except for the 300 V, 6.3 kW, 1.25x magnetic field strength condition, the energy trends were in excellent agreement across the two tests. As was the case with the TDU1, the low-energy ions near the IFPC of ETU2 exhibited increasing energy with increasing magnetic field strength. Furthermore, from Table 6, the newly identified medium-energy ions near the IFPC exhibited an even more pronounced increase in energy with magnetic field strength, with the caveat that the number of samples was low. Interestingly, from Table 7, the energy of the OFPC ions appear relatively constant with changing magnetic field strength, though analysis shows that the percentage of ions above 50 eV rose with rising magnetic field strength. OFPC ions for TDU1 exhibited a clear rise in energy with magnetic field strength [7]. Notably, cathode ions were also observed to have increasing energy with increasing magnetic field strength in a stand-alone cathode test [26].

D. ETU to TDU comparison – Flow rate throttling

The data set for comparing ETU2 to TDU1 in terms of flow rate throttling (throttling discharge power by keeping discharge voltage constant and varying anode mass flow rate) was limited since the two thrusters were not tested at the same conditions. Nevertheless, comparisons of the general trends with flow rate throttling can be made to inform whether the thrusters operate with similar discharge physics.

Figure 32 shows the averaged axial velocity of the ions along discharge channel centerline for the flow rate throttling study performed on the ETU2 in VF5. Figure 33 shows the same type of plot for the TDU1 in VF6 at the same discharge voltage [13]. Like TDU1, the acceleration zone of the ETU2 moved upstream as the discharge power (and flow rate) decreased and became stretched out at less than a quarter of the nominal discharge power.
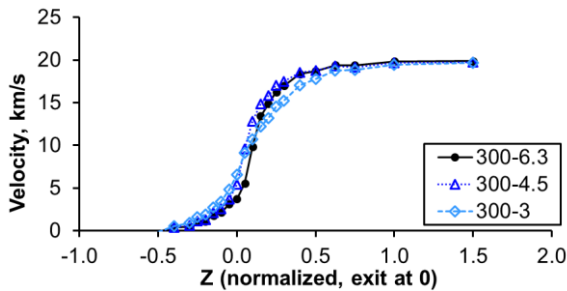

Figure 32. Averaged axial ion velocity along discharge channel centerline for the ETU2 operating at 300 V and varying discharge power.
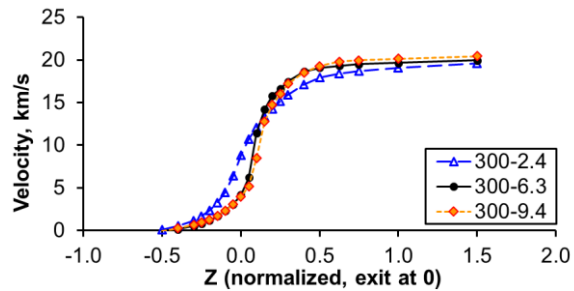
Figure 33. Averaged axial ion velocity along discharge channel centerline for the TDU1 operating at 300 V and varying discharge power [13].

Figures 34 and 35 show the averaged ion velocity vector near the IFPC and OFPC, respectively, of the ETU2 operating at 300 V, 3 kW. Figures 36 and 37 show same type of plots for the ETU2 operating at 300 V, 4.5 kW. The medium-energy IFPC population (green arrow) could be picked out at a greater number of locations for the 3-kW condition than for the 4.5-kW condition.

15

Table 8 summarizes the energy and angle characteristics of the low-energy stream from the discharge channel and the stream from the cathode for the flow rate throttling study. Averaging was performed over the same IFPC locations as for Table 2. Table 9 and Table 10 summarize the same parameters for the medium-energy population from the discharge channel arriving at the IFPC and OFPC, respectively. For Table 9, averaging was performed for data locations at which data was obtained at all listed operating conditions to account for the fact that the medium-energy peak was not detected at many data locations for some conditions.
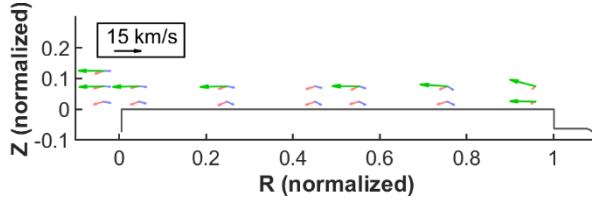

Figure 34. Averaged velocity vector near the IFPC for ETU2 operating at 300 V, 3 kW.
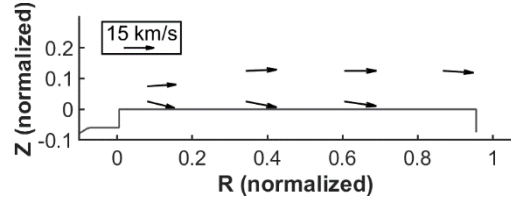

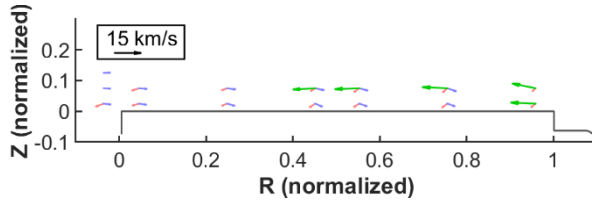**Figure 35. Averaged velocity vector near the OFPC for ETU2 operating at 300 V, 3 kW.**

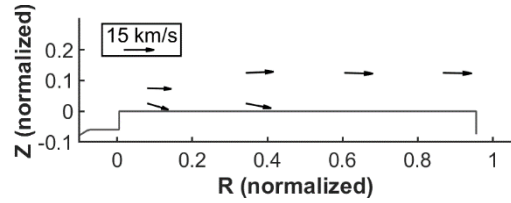**Figure 36. Averaged velocity vector near the IFPC for ETU2 operating at 300 V, 4.5 kW.**

Figure 37. Averaged velocity vector near the OFPC for ETU2 operating at 300 V, 4.5 kW.

Table 8. IFPC ion characteristics for the ETU2 magnetic variation studies.

Condition	Sample Size	Discharge Channel Low-Energy Stream				Cathode Stream			
		E_{AVG}, eV	E_{FWHM}, eV	% above 50 eV	AOI_{AVG}, degree	E_{AVG}, eV	E_{FWHM}, eV	% above 50 eV	AOI_{AVG}, degree
300-3	10	30	39	14.3	64	23	31	7.9	63
300-4.5	10	18	23	3.1	52	23	31	5.9	70
300-6.3	18	22	25	4.1	48	26	32	8.8	63

Table 9. Third IFPC ion characteristics for the ETU2 magnetic variation studies

Condition	Sample Size	E_{AVG}, eV	E_{FWHM}, eV	% above 50 eV	AOI_{AVG}, degree
300-3	4	165	86	100.0	97
300-4.5	4	138	61	100.0	95
300-6.3	4	145	96	99.6	94

Table 10. OFPC ion characteristics for the ETU2 magnetic variation studies

Condition	Sample Size	E_{AVG}, eV	E_{FWHM}, eV	% above 50 eV	AOI_{AVG}, degree
300-3	7	163	78	100.0	85
300-4.5	6	121	79	97.5	84
300-6.3	11	119	90	96.8	79

From the above tables, one can see the ion characteristics were similar between the 300 V, 4.5 kW and 300 V, 6.3 kW. However, when throttling down to 3 kW, the energies of the two populations from the discharge channel as well as the one population found near the OFPC (also from the discharge channel) increased noticeably. One possibility was that as acceleration moved upstream with decreasing mass flow, the energetic downstream part of the plasma plume became closer to the pole cover. Another possibility was that the mechanism responsible for energizing the above-mentioned ions is dampened by the presence of neutrals. This trend would also explain the reduction in energy

of the medium-energy IFPC population with increasing background pressure. A similar increase in energy was also observed in the TDU1 during the LIF study in VF6 [13].

E. Cathode flow fraction study

During the ETU2 LIF test, a cathode flow fraction study was performed. Figure 38 shows the averaged axial velocity of the ions along discharge channel centerline for the thruster operating at 600 V, 12 kW and different cathode flow fractions. For this study, the lowest tested cathode flow fraction will be referred to as the "base CFF" and all other cathode flow fraction values will be listed as multiples of base CFF. From this figure, one can see that the ion characteristics shown were identical to within experimental uncertainties.

An examination of the discharge channel ion velocity vectors shows that the vectors were nearly identical between the 600 V, 12 kW, 1X and 1.75X lowest cathode flow fraction conditions and the variation in cathode flow fraction did not noticeably affect the vectors of the ions found in the discharge channel region. On the other hand, the cathode flow rate had a measurable impact on the ions found near the IFPC.
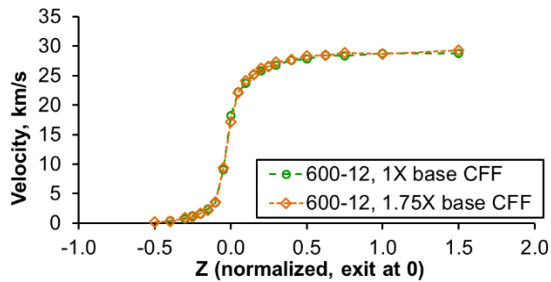

Figure 38. Averaged axial ion velocity along discharge channel centerline for ETU2 at 600 V, 12 kW, and different cathode flow fractions.

Figure 39. Averaged velocity vector near the IFPC for ETU2 operating at 600 V, 12 kW, 1X base CFF.
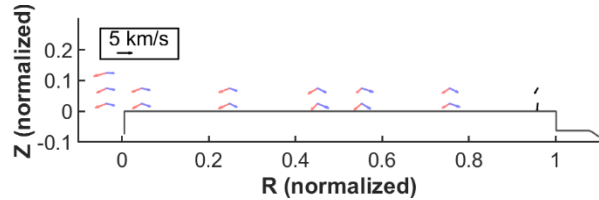
Figure 40. Averaged velocity vector near the IFPC for ETU2 operating at 600 V, 12 kW, 1.75X base CFF.

Figure 39 and Figure 40 show the averaged ion velocity vector near the IFPC of the ETU2 operating at 600 V, 12 kW, 1X and 1.75X base CFF, respectively. No medium-energy ion populations were found near the IFPC at these conditions. Ions were detected at 1-3 locations near the OFPC and was not shown due to the small size of the data set.
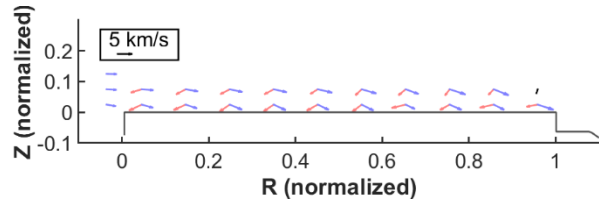
Table 11 summarizes the ion energy and angle characteristics of the low-energy streams from the discharge channel and cathode for the cathode flow fraction study. Averaging was performed over the same IFPC locations as for Table 2. Comparing operations at 1X and 1.75X base CFF, the cathode ions became less energetic as the cathode flow rate increased. The energy of the cathode stream was much lower at the higher cathode flow condition, with the percentage of ions with energy above 50 eV falling from ~5% to ~1%. Interestingly, the energy of the discharge channel low-energy ions also dropped, though not by as much as the cathode stream ions. This data strongly supported the hypothesis that the stream of ions moving radially outward across the IFPC had in fact come from the cathode as opposed to other sources (e.g. ions crossing over the central axis of the thruster). The trend of decreasing ion energy with increasing cathode flow rate was also observed in a stand-alone cathode test [26].

Table 11. IFPC ion characteristics for the ETU2 operating at 600 V, 12 kW with different cathode flow fractions.

Condition	Sample Size	Discharge Channel Low-Energy Stream				Cathode Stream			
		E_{AVG}, eV	E_{FWHM}, eV	% above 50 eV	AOI_{AVG}, degree	E_{AVG}, eV	E_{FWHM}, eV	% above 50 eV	AOI_{AVG}, degree
600-12, 1X base CFF	18	18	22	1.5	51	22	28	4.7	65
600-12, 1.75X base CFF	10	14	16	0.3	50	14	19	0.8	60

F. Third IFPC population and relation to erosion-enhancing plasma waves

The bulleted list below summarizes the characteristics of the medium-energy IFPC population found in this ETU2 LIF test:

- These medium-energy ions were identified for the thruster operating at 300 V condition but not at higher discharge voltages.
- These ions were easiest to identify at low mass flow rate (low discharge power).
- These ions appeared to increase in energy with magnetic field strength.
- These ions appeared to increase in energy with decreasing background pressure.
- These ions had very similar energy to the ions near the OFPC and appeared to move in the opposite direction as the OFPC ions.

One hypothesis is that the third IFPC population was energized by the same mechanism that produced the energetic OFPC ions. Given that the ETU has channel geometries and magnetic fields that are roughly symmetric about the discharge channel centerline, it is not surprising that same mechanism may be at work in both the outer chamfer and the inner chamfer regions. Indeed, it was a bigger surprise to not have found these medium-energy ions in the earlier TDU1 test in VF6. The improved SNR of the current LIF system was likely a contributor to being able to identify this medium-energy IFPC population.

The leading hypotheses for the mechanism responsible for creating these energetic ions are lower hybrid plasma waves. Mikellides and Lopez Ortega proposed two different lower hybrid waves that are good candidates for the collected data, while also identifying other candidate waves that could play roles in enhancing pole erosion [11, 27]. Analysis to determine which plasma wave is a better fit as the mechanism for energizing the third IFPC population is left for future work. For this paper, we will start with a simpler assumption, which is that a plasma wave of some kind that involves magnetized electrons was responsible for energizing and scattering ions in the chamfer region and examine how well this assumption fits the data.

From Mikellides and Lopez Ortega's work [11], lower hybrid plasma waves are prime candidates because they only exist in the presence of magnetized electrons. From the LIF data in this test and the TDU1 test, prominent VDF broadening was found in the plasma near the chamfer region, where magnetic field strength tends to be very high compared to the rest of the discharge channel. If the mechanism is a plasma involving magnetized electrons, it would explain why the medium-energy ion population tended to be most easy to identify at the IFPC location nearest to the chamfer. The fact that the energy of the medium-energy IFPC ions increased with magnetic field strength can be explained by the idea that the assumed plasma wave is powered by magnetized electrons (i.e. higher magnetic field strength leads to higher electron temperature, which leads to greater energy transfer to the originally low-energy ions). One caveat is that while the electrons have been known to reach tens of eV in the discharge channel [11], they do not reach the 100+ eV seen in the medium-energy ion population, nor would the electrons' heating create large directed velocity component. It is possible that the plasma wave not only contributes VDF broadening to the medium-energy ion population, but also caused some of them to take a more divergent trajectory out of the discharge channel. As these ions traverse the more divergent trajectory, they gain a portion of the acceleration as they drop down the electrostatic potential, thus they emerge from the chamfer region with broadened VDF, a highly radial vector, and a fraction of the discharge potential.

If the mechanism was a plasma wave with magnetized electrons, the observed trend with mass flow rate and background pressure can be explained by the fact that background neutrals moderates the energy of the electrons and dampens the magnitude of the plasma wave. Since both reducing flow rate and reducing background pressure reduces neutral density, the energy of the medium-energy IFPC ions should increase in both scenarios, as was observed in the experiment. Interestingly, reducing flow rate caused the acceleration zone to move upstream while reducing background pressure caused the acceleration zone to move downstream. These data support the idea that the change in energy of the medium-energy IFPC ions could not be entirely attributed to shifting acceleration zone.

If the mechanism was a plasma wave with magnetized electrons, high magnetic field strength would have been required to energize the ions, one would expect the amount of energetic ions produced to scale with the amount of low energy ions that enter the near-chamfer region. For the ETU and TDU, the main beam was much less divergent at high discharge voltage conditions [7, 28]. This trend likely means that less ions enter the near-chamfer region for 600 V operations than for 300 V operations. Indeed, a study performed during the VF6 TDU1 test showed that some data could be collected from near the chamfers at 300 V, 6.3 kW condition but not at the 600 V, 12.5 kW condition [28]. If less ions were entering the near-chamfer region during 600 V operation than during 300 V operation, then less medium-energy ions would have been detectable on both the IFPC and the OFPC, which matches the experimental observations. Additionally, TDU and ETU wear tests have shown that erosion rates for both IFPC and OFPC were notably higher at 300 V operating conditions than at 600 V operating conditions [16, 29]. The difference in erosion

rates might be partly attributable to the changing characteristics of these medium-energy ions at the two discharge voltages.

From the above thought experiment, the experimental data appeared to fit well with the hypothesis that the medium-energy ions near the IFPC and OFPC were created from plasma wave heating and scattering. There is still an outstanding question of exactly how much these ions contribute to the erosion of the inner pole cover. Arguments for the importance of the medium-energy ions in erosion includes: these ions have high energy well in excess of what can cause erosion; these ions were the only population measured near the OFPC and the OFPC is known to erode [16]; and characteristics of the measured medium-energy ions trend as expected with wear rate measured at different discharge voltage operations. Arguments against these ions contributing to IFPC erosion includes: these ions appeared to be very small in number (though OFPC ions were also small in number yet still appeared to cause erosion); and these ions appeared to be aimed slightly away from the pole cover (though a small fraction is still expected to reach the pole cover due to spread in VDFs).

V. Conclusions

The ETU2 LIF test in VF5 has been successfully completed. Comparison of the data to TDU data sets show that the ETU and TDU have nearly identical ion production and acceleration characteristics. Comparison of data across test facilities showed that there were only minor differences in the behavior of the plasma with different facilities. The background pressure study showed that the acceleration zone of the ETU2 moved upstream with increasing background pressure by amounts that were similar to the TDU1. The magnetic variation study showed that the acceleration zone of the ETU2 moved upstream with increasing magnetic field strength, just like the TDU1. The flow rate throttling study showed that the acceleration zone of the ETU2 moved upstream with decreasing mass flow rate, same as the TDU1.

Examinations of the low-energy ions near the IFPC arriving from the discharge channel and cathode showed that the characteristics of the ions did not vary much with background pressure (within the tested pressure range). However, these ions did become more energetic with increasing magnetic field strength, and their energy increased greatly when the thruster was throttled down to a quarter of the maximum discharge power. Furthermore, the cathode stream of ions appeared to be highly sensitive to the cathode flow fraction and became less energetic with increasing cathode flow fraction. For these ions, with averaged energies of 20-30 eV and FWHM energies of 30-40 eV, up to 15% of the VDF have energies exceeding 50 eV before accounting for energy from sheath drop. As with the TDU1, these ETU2 near-pole ions were found to impact the pole covers at high oblique angles.

Examination of the medium-energy ions near the IFPC showed that these ions were much easier to identify for operations at 300 V than at higher discharge voltages. Their energy appeared to increase with decreasing mass flow and background pressure, and also increase with increasing magnetic field strength. Their characteristics were highly similar to the single ion population found near the OFPC and the two populations exhibited very similar trends with different control parameters. These two medium-energy populations (one near IFPC and one near OFPC) had averaged energies of 100-170 eV and FWHM energies of 80-110 eV. These medium energy ions were much more energetic than the low-energy IFPC ions but also much lower in intensity in the LIF scans, which roughly correlated to lower densities.

Put together, the above data sets suggested that accurate predictions of IFPC erosion rate at 300 V operating conditions for the ETU may require accurate accounting of all three ion populations present near the IFPC. Though predicting IFPC erosion for 600 V operations will likely be easier given the medium-energy population was absent from the IFPC data and only showed up in a small number of scans in the OFPC data.

References

[1] Congress, "National Aeronautics and Space Administration Transition Authorization Act of 2017", 2017.

[2] SpaceNews. *NASA refines plans for launching Gateway and other Artemis elements*. 2020 May 14 [cited; Available from: https://spacenews.com/nasa-refines-plans-for-launching-gateway-and-other-artemis-elements/.

[3] NASA. *NASA Awards Artemis Contract for Lunar Gateway Power, Propulsion*. 2019 [cited; Available from: https://www.nasa.gov/press-release/nasa-awards-artemis-contract-for-lunar-gateway-power-propulsion.

[4] Herman, D. A., Gray, T. G., Johnson, I., Kerl, T., Lee, T., and Silva, T., "The Application of Advanced Electric Propulsion on the NASA Power and Propulsion Element (PPE)", *36th International Electric Propulsion Conference*, 2019-651, Vienna, Austria, Sep 15-20, 2019.

[5] Smith, B. K., Nazario, M. L., and Cunningham, C. C., "Solar Electric Propulsion Vehicle Demonstration to Support Future Space Exploration Missions", *Space Propulsion 2012*, Bordeaux, France, May 7-10, 2012.

[6] Hofer, R. R., Lobbia, R. B., Chaplin, V. H., Lopez Ortega, A., Mikellides, I. G., Polk, J. E., Kamhawi, H., Frieman, J. D., Huang, W., Peterson, P. Y., and Herman, D. A., "Completing the Development of the 12.5 kW Hall Effect Rocket with Magnetic Shielding (HERMeS)", *36th International Electric Propulsion Conference*, 2019-193, Vienna, Austria, Sep 15-20, 2019.

[7] Huang, W. and Kamhawi, H., "Counterstreaming ions at the inner pole of a magnetically shielded Hall thruster", *Journal of Applied Physics*, Vol. 129, Jan 27, 2021, pp. 043305. https://doi.org/10.1063/5.0029428

[8] Frieman, J. D., Kamhawi, H., Mackey, J. A., Haag, T. W., Peterson, P. Y., Herman, D. A., Gilland, J. H., and Hofer, R. R., "Completion of the Long Duration Wear Test of the NASA HERMeS Hall Thruster", *2019 AIAA Propulsion and Energy Forum*, AIAA-2019-3895, Indianapolis, IN, Aug 19-22, 2019. https://doi.org/10.2514/6.2019-3895

[9] Kamhawi, H., Huang, W., Gilland, J. H., Haag, T. W., Mackey, J. A., Yim, J. T., Pinero, L. R., Williams, G. J., Peterson, P. Y., and Herman, D. A., "Performance, Stability, and Plume Characterization of the HERMeS Thruster with Boron Nitride Silica Composite Discharge Channel", *35th International Electric Propulsion Conference*, 2017-392, Atlanta, GA, Oct 8-12, 2017.

[10] Lopez Ortega, A., Mikellides, I. G., Chaplin, V. H., Huang, W., and Frieman, J. D., "Anomalous Ion Heating and Pole Erosion in the 12.5-kW Hall Effect Rocket with Magnetic Shielding (HERMeS)", *2020 AIAA Propulsion and Energy Forum*, AIAA-2020-3620, Virtual, Aug 24-28, 2020. https://doi.org/10.2514/6.2020-3620

[11] Mikellides, I. G. and Lopez Ortega, A., "Growth of the modified two-stream instability in the plume of a magnetically shielded Hall thruster", *Physics of Plasmas*, Vol. 27, No. 10, Oct 5, 2020, pp. 100701. https://doi.org/10.1063/5.0020075

[12] Peterson, P. Y., Kamhawi, H., Huang, W., Yim, J. T., Herman, D. A., Williams, G. J., Gilland, J. H., and Hofer, R. R., "NASA's HERMeS Hall Thruster Electrical Configuration Characterization", *52nd AIAA/SAE/ASEE Joint Propulsion Conference*, AIAA-2016-5027, Salt Lake City, UT, Jul 25-27, 2016. https://doi.org/10.2514/6.2016-5027

[13] Huang, W., Kamhawi, H., and Peterson, P. Y., "Effects of Background Pressure and Electrical Configuration on the Velocity Field of the HERMeS Hall Thruster", *2020 AIAA Propulsion and Energy Forum*, AIAA-2020-3616, Virtual, Aug 24-28, 2020. https://doi.org/10.2514/6.2020-3616

[14] Jackson, J., Miller, S., Cassady, J., Soendker, E., Welander, B., Barber, M., and Peterson, P. Y., "13kW Advanced Electric Propulsion Flight System Development and Qualification", *36th International Electric Propulsion Conference*, 2019-692, Vienna, Austria, Sep 15-20, 2019.

[15] Frieman, J. D., Kamhawi, H., Huang, W., Mackey, J. A., Ahern, D. M., Peterson, P. Y., Gilland, J. H., Hall, S. J., Hofer, R. R., Inaba, D., Dao, H., Zubair, J., Neuhoff, J., and Branch, N. A., "Characterization Test of the 12.5-kW Advanced Electric Propulsion System Engineering Test Unit Hall Thruster", *2020 AIAA Propulsion and Energy Forum*, AIAA-2020-3626, Virtual, Aug 24-28, 2020. https://doi.org/10.2514/6.2020-3626

[16] Frieman, J. D., Kamhawi, H., Huang, W., Mackey, J. A., Ahern, D. M., Peterson, P. Y., Gilland, J. H., Hall, S. J., Hofer, R. R., Inaba, D., Dao, H., Zubair, J., Neuhoff, J., and Branch, N. A., "Wear Test of the 12.5-kW Advanced Electric Propulsion System Engineering Test Unit Hall Thruster", *2020 AIAA Propulsion and Energy Forum*, AIAA-2020-3625, Virtual, Aug 24-28, 2020. https://doi.org/10.2514/6.2020-3625

[17] Yim, J. T. and Burt, J. M., "Characterization of Vacuum Facility Background Gas Through Simulation and Considerations for Electric Propulsion Ground Testing", *51st AIAA/SAE/ASEE Joint Propulsion Conference*, AIAA-2015-3825, Orlando, FL, Jul 27-29, 2015. https://doi.org/10.2514/6.2015-3825

[18] Hansen, J. and Persson, W., "Revised Analysis of Singly Ionized Xenon, Xe II", *Physica Scripta*, Vol. 36, No. 4, 1987, pp. 602-643. https://doi.org/10.1088/0031-8949/36/4/005

[19] Huang, W., Smith, T. B., and Gallimore, A. D., "Obtaining Velocity Distribution using a Xenon Ion Line with Unknown Hyperfine Constants", *40th AIAA Plasmadynamics and Laser Conference*, AIAA-2009-4226, San Antonio, Texas, Jun 22-25, 2009. https://doi.org/10.2514/6.2009-4226

[20] Huang, W., "Singly-Charged Xenon Zeeman Effect Study Results and Validation," in *Study of Hall Thruster Discharge Channel Wall Erosion via Optical Diagnostics*, University of Michigan, Ann Arbor, MI, 2011, pp. 59-62.

[21] Huang, W., "Multi-peaked Velocity Distribution Functions," in *Study of Hall Thruster Discharge Channel Wall Erosion via Optical Diagnostics*, University of Michigan, Ann Arbor, MI, 2011, pp. 127-130.

[22] Yim, J. T., "A survey of xenon ion sputter yield data and fits relevant to electric propulsion spacecraft integration", *35th International Electric Propulsion Conference*, 2017-060, Atlanta, GA, Oct 8-12, 2017.

[23] Chaplin, V. H., Jorns, B. A., Conversano, R. W., Lobbia, R. B., Lopez Ortega, A., Mikellides, I. G., and Hofer, R. R., "Laser Induced Fluorescence Measurements of the Acceleration Zone in the 12.5 kW HERMeS Hall Thruster", *35th International Electric Propulsion Conference*, 2017-229, Atlanta, GA, Oct 8-12, 2017.

[24] Chaplin, V. H., Lobbia, R. B., Lopez Ortega, A., Mikellides, I. G., Roberts, P. J., Peter, J. S., Hofer, R. R., Polk, J. E., and Friss, A. J., "Spatiotemporally Resolved Ion Velocity Distribution Measurements in the 12.5 kW HERMeS Hall Thruster", *36th International Electric Propulsion Conference*, 2019-532, Vienna, Austria, Sep 15-20, 2019.

[25] Huang, W., Kamhawi, H., and Herman, D. A., "Evidence of Counter-Streaming Ions near the Inner Pole of the HERMeS Hall Thruster", *2019 AIAA Propulsion and Energy Forum*, AIAA-2019-3897, Indianapolis, IN, Aug 19-22, 2019. https://doi.org/10.2514/6.2019-3897

[26] Hall, S. J., Gray, T. G., Yim, J. T., Choi, M., Mooney, M. M., Sarver-Verhey, T. R., and Kamhawi, H., "The Effect of a Hall Thruster-like Magnetic Field on Operation of a 25-A class Hollow Cathode", *36th International Electric Propulsion Conference*, 2019-300, Vienna, Austria, Sep 15-20, 2019.

[27] Mikellides, I. G. and Lopez Ortega, A., "Growth of the lower hybrid drift instability in the plume of a magnetically shielded Hall thruster", *Journal of Applied Physics*, Vol. 129, No. 19, May 17, 2021, pp. 193301. https://doi.org/10.1063/5.0048706

[28] Huang, W., Kamhawi, H., and Herman, D. A., "Ion Velocity in the Discharge Channel and Near-Field of the HERMeS Hall Thruster", *2018 Joint Propulsion Conference*, AIAA-2018-4723, Cincinnati, OH, Jul 9-11, 2018. https://doi.org/10.2514/6.2018-4723

[29] Frieman, J. D., Kamhawi, H., Williams, G. J., Herman, D. A., Peterson, P. Y., Gilland, J. H., and Hofer, R. R., "Long Duration Wear Test of the NASA HERMeS Hall Thruster", *2018 Joint Propulsion Conference*, AIAA-2018-4645, Cincinnati, OH, Jul 9-11, 2018. https://doi.org/10.2514/6.2018-4645